



Cite this: *Phys. Chem. Chem. Phys.*,  
2025, 27, 7929

# When carbon monoxide goes “upside down”: vibrational signatures of CO at NaCl(100) from *ab initio* molecular dynamics†

Shreya Sinha, \*<sup>a</sup> Alec M. Wodtke <sup>bc</sup> and Peter Saalfrank \*<sup>a</sup>

CO adsorbed on NaCl(100) is a model system for surface science showing a rich variety of interesting phenomena. It features several adsorption phases like tilted/antiparallel or perpendicular/upright, very long vibrational lifetimes of the CO internal stretch (IS) mode, anharmonicity-driven vibrational energy pooling, “C-bound” vs. “O-bound” adsorption, and heavy-atom gateway tunneling during CO inversion at low temperatures. Typically, these features and phenomena are experimentally probed by stationary and time-resolved vibrational spectra, exhibiting characteristic differences between the various adsorption modes and phases. To gain atom- and time-resolved insight into vibrational response of CO molecules on NaCl(100), vibrational density of states (VDOS), infrared (IR) and vibrational sum frequency (VSF) spectra are computed from velocity velocity correlation functions (VVCFs) by *ab initio* molecular dynamics (AIMD) for various coverages, temperatures and phases. In agreement with experiments, we find that increasing CO (“C-bound”) coverages as well as CO inversion lead to redshifts of the CO IS mode. We predict more diffuse spectra at  $T = 300$  K compared to 30 K, reflecting the disorder of adsorbates and monolayer instability at room temperature. Analyzing molecularly decomposed and internal VDOS curves as well as computed non-linear correlation matrices give further insight into the complex molecular dynamics underlying the vibrational spectra, notably for the low-frequency regime where frustrated rotations, translations and intermolecular motions come into play. On a methodological side, we also test and discuss some intricate details of how to compute IR and VSF response using a modified formulation of the VVCF methods [Ohto *et al.*, *J. Chem. Phys.*, 2015, **143**, 124702], by including time and angle-dependent dipole and polarizability derivatives as well as intermolecular couplings by cross correlations. Their effect on computed vibrational spectra is studied. These findings provide a detailed, microscopic insight into the picosecond vibrational spectra and dynamics of CO on NaCl(100), highlighting the effects of temperature, coverage, and changes in adsorbate orientation.

Received 11th December 2024,  
Accepted 26th March 2025

DOI: 10.1039/d4cp04671d

rsc.li/pccp

## 1 Introduction

CO on a NaCl(100) surface is a well-known and long-studied model system for adsorption. However, recent new findings

demonstrate that this system is still good for surprises, with new structures and phenomena emerging. Many of these phenomena are due to the fact that CO interacts only weakly with NaCl(100), making it an ideal microlab to study intermolecular interactions.

Experimentally it is known that, at a coverage of 1 ML ( $\theta = 1$ , one CO per surface Na<sup>+</sup>), a  $(1 \times 1)$  “parallel/upright” (P/U) phase with C atoms pointing downward (to Na<sup>+</sup>) is the most stable phase above 35 K. Below this temperature a  $p(1 \times 1)$  P/U  $\rightarrow$   $p(2 \times 1)$  T/A phase transition occurs, with T/A denoting a “tilted/antiparallel” orientation.<sup>1</sup> Both phases are shown in Fig. 1. Density functional theory (DFT) confirmed that indeed, the most stable monolayer phase of CO/NaCl(100) at low temperatures is T/A.<sup>2–4</sup> P/U is favoured at higher  $T$  for  $\theta = 1$ , but also found at low, sub-monolayer coverages, even at low  $T$  according to theory. For example, at  $\theta = 1/8$ , P/U is most stable according to density functional calculations and beyond.<sup>4</sup>

<sup>a</sup> Theoretical Chemistry, Institute of Chemistry, University of Potsdam, Karl-Liebknecht-Str. 24-25, 14476 Potsdam, Germany. E-mail: [sinha@uni-potsdam.de](mailto:sinha@uni-potsdam.de), [peter.saalfrank@uni-potsdam.de](mailto:peter.saalfrank@uni-potsdam.de); Tel: +49 (0)331-977-6138, +49 (0)331-977-5232

<sup>b</sup> Department of Dynamics at Surfaces, Max-Planck-Institute for Multidisciplinary Sciences, Am Fassberg 11, 37077 Göttingen, Germany

<sup>c</sup> Institute for Physical Chemistry, University of Göttingen, Tammannstr. 6, 37077 Göttingen, Germany

† Electronic supplementary information (ESI) available: Technical details on AIMD calculations, computation of VVAFs, VDOS in internal coordinates, anisotropy inclusions in dipole and polarizability derivatives to compute IR and VSF spectra; normal modes and vibrational free energies; testing methodological variants and inclusion of cross-correlations for computing IR and VSF spectra; analysis of trajectories (mode correlations, diffusion and orientation dynamics). See DOI: <https://doi.org/10.1039/d4cp04671d>



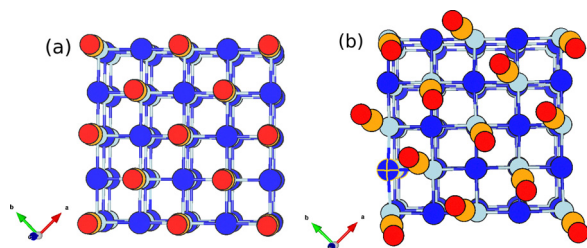


Fig. 1 (a) Parallel/upright (PU) and (b) tilted/parallel (T/U) phases for monolayer CO/NaCl(100). The coloured balls, yellow, red, light blue and dark blue correspond to C, O, Na, and Cl atoms, respectively.

Such structural details and their changes are typically explored experimentally by various forms of vibrational spectroscopy, in particular the CO stretching mode being a sensitive reporter mode.<sup>1,5,6</sup> Specifically, at a coverage  $\theta = 1$  (1 ML) and  $T = 40$  K, where the P/U phase dominates, experimentally a single CO peak at  $2155\text{ cm}^{-1}$  was found. At temperatures below the  $p(1 \times 1)$  P/U  $\rightarrow$   $p(2 \times 1)$  T/A transition, a minor peak appears at around  $2149\text{ cm}^{-1}$ , and the original peak slightly shifts (by  $<1\text{ cm}^{-1}$ ) to the red.<sup>1</sup> This second peak has been interpreted as being due to exciton (Davydov) splitting by  $\Delta_D \sim 6\text{ cm}^{-1}$ , arising from interacting vibrational transition dipole moments of the CO molecules in the T/A phase.<sup>7</sup>

In another more recent work, Lau *et al.*<sup>8</sup> reported polarized Fourier transformed infrared (FTIR) absorption spectra as a function of coverage between 0.02 and 1.0 ML. They found that even at temperatures as low as 30 K, non-equilibrium structures exist, which broaden the monolayer spectra, indicative of diffusion and island formation. Tilt angles of adsorbed CO as a function of coverage were also extracted, which show an abrupt change between 0.2 and 0.3 ML from  $0^\circ$  (upright) to  $\sim 30^\circ$  (tilted) for higher coverages, this way supporting the mentioned preference of P/U at low coverage.

In further work, Wodtke and coworkers found by IR fluorescence spectroscopy that, for a CO overlayer buried under a CO adsorbate layer at 7 K, it is possible to flip C-bound CO molecules in the CO monolayer by highly exciting the C–O bond, to an “O-bound” form, *i.e.*, (some of the) CO molecules underwent an isomerization to an “upside-down” configuration.<sup>9</sup> The highly vibrationally excited CO molecules (with  $\nu = 20$ – $30$  vibrational quanta) had been created by IR excitation of adsorbed CO from  $\nu = 0$  to  $\nu = 1$  and subsequent vibrational energy pooling (VEP), *i.e.*, vibrational-energy transfer events of the type  $\text{CO}(\nu) + \text{CO}(\nu) \rightarrow \text{CO}(\nu - 1) + \text{CO}(\nu + 1)$ . VEP is driven by dipole-dipole coupling between CO molecules and the anharmonicity of the CO vibrational potential,<sup>10,11</sup> in combination with extraordinary long vibrational lifetimes (on the order of ms) of CO adsorbed on NaCl(100). The latter is due to the mentioned, weak interaction of CO with the surface. It was also found that the C–O vibration of O-bound species, once formed, was red-shifted by about  $\Delta = 15\text{ cm}^{-1}$  compared to C-bound.<sup>9</sup> In even more recent work,<sup>12,13</sup> they further observed, again by vibrational spectroscopy, that even at low temperatures (around 20 K) the back-reaction of “O-bound” to “C-bound” occurs, which could be

explained qualitatively *via* a phonon-assisted resonant heavy-atom tunneling mechanism involving “gateway states”.

From the theory side, vibrational properties and spectra of CO molecules at NaCl(100) were mostly studied so far by stationary normal mode analysis, NMA, which neglects anharmonicity and inter-mode couplings and finite temperature.<sup>4,14–16</sup> This necessitates dynamical calculations which allow for real-time, atom-resolved insight and additionally include anharmonicity, intramolecular and intermolecular mode couplings and finite temperature effects in simulated vibrational spectra. Below we report an in-depth analysis of vibrational spectra for different phases of CO, both “C-bound” and “O-bound”, on NaCl(100) at different coverages (0.25, 0.5, and 1 ML), and at two different temperatures ( $T = 30\text{ K}$ ,  $300\text{ K}$ ), *i.e.*, below and above the T/A  $\rightarrow$  P/U phase transition at higher coverages. To do so, we use an *ab initio* molecular dynamics–velocity velocity correlation function (AIMD–VVCF) approach.

Our paper is organized as follows. Section 2 outlines models and methods used for computing the vibrational spectra and deriving dynamic properties. Section 3 presents results in different subsections dealing with the different kinds of vibrational signatures (vibrational density of states (VDOS), InfraRed (IR) and vibrational sum frequency (VSF) spectra), for some selected initial configurations and their dependence on coverage and temperature. A final section summarizes this work. Many numerical details and additional results can be found in the ESI.†

## 2 Methods and models

### 2.1 Electronic structure method and adopted models

In what follows, periodic supercell calculations using periodic DFT, employing the PBE exchange correlation functional<sup>17</sup> and standard pseudopotentials with a projector augmented wave (PAW) basis,<sup>18</sup> as implemented in the Vienna *ab initio* Simulation (VASP) Package,<sup>19–22</sup> were carried out. Grimme’s D2 correction<sup>23</sup> was applied to account for van der Waals interactions. For all calculations, we used a  $2 \times 2 \times 1$   $\Gamma$ -centered  $k$ -point mesh and a kinetic energy cutoff of 700 eV.

The specific surface models, some of them analogous to ref. 16, are all based on  $2\sqrt{2} \times 2\sqrt{2} \times 3$  supercells, with dimensions  $8.017 \times 8.017 \times 30\text{ \AA}$  ( $\sim 20\text{ \AA}$  vacuum along  $z$ , the direction perpendicular to the surface), if not stated otherwise. Different models were chosen and geometry-optimized, serving for normal mode analysis (NMA) and *ab initio* molecular dynamics (AIMD) – see below. For geometry optimizations, the upper surface layer and the CO molecules were relaxed. Fig. 2 shows six different, geometry-optimized models A–F:

- Model A corresponds to coverage  $\theta = 1/4$  (one of four Na<sup>+</sup> ions in the upper layer occupied by CO, with “C-down”); note that CO is ideally “upright”.
- Model B corresponds to coverage  $\theta = 1/2$  with both CO molecules “C-bound”, and being tilted.
- Model C corresponds to  $\theta = 1$ , in the most stable T/A phase with all CO molecules “C-bound” and tilted.



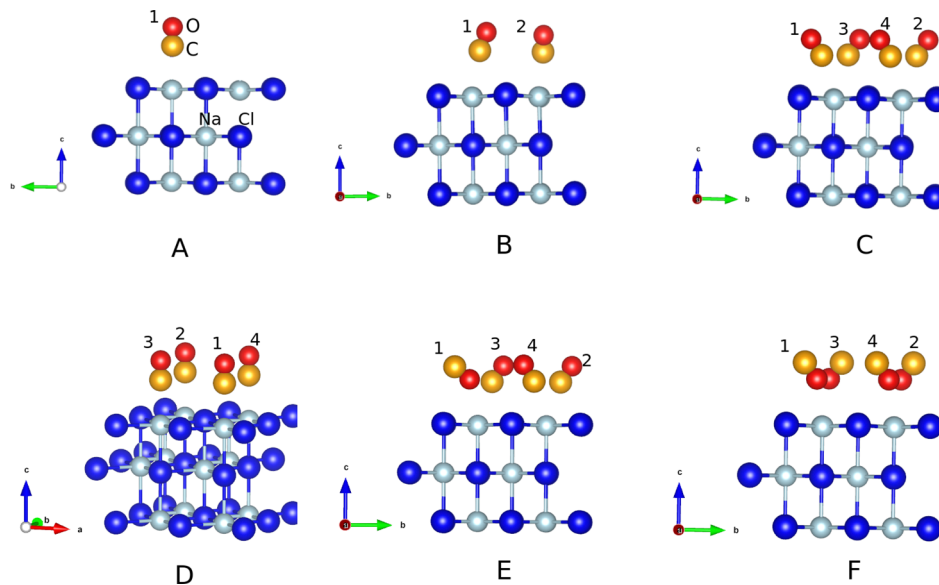


Fig. 2 Optimized (PBE+D2) structures for various adsorbate models for CO/NaCl(100) – see text. (A) and (B) are low-coverage where (A) is in the P/U and (B) in the T/A phase, (C)–(F) are high-coverage ( $\theta = 1$ ) models, all being in the T/A phase.

- Model D is a metastable form for  $\theta = 1$  at low  $T$ , the P/U structure with all CO molecules parallel and upright. P/U is found to be 0.02 eV per CO molecule (0.08 eV in total) higher in energy than the T/A phase C, on the PBE+D2 level of theory.

- Model E corresponds also to  $\theta = 1$ , however, with one of the four CO molecules (denoted  ${}^1\text{CO}$ ) inverted to “O-bound”. This form is 0.084 eV higher in energy than the T/A model C.

- Model F corresponds again to  $\theta = 1$ , now, however, all four CO molecules are “O-bound”. On the PBE+D2 level, the corresponding energy is 0.085 eV per CO molecule higher in energy than form C, showing that the inversion energy per CO depends only marginally on the number of molecules which are inverted.

- In addition, (not shown in Fig. 2) a model G was considered, derived from model E by adding two CO overlayers on top of the adsorbate layer. Model G is a candidate structure for the mentioned experiments<sup>9,13</sup> with “buried” adsorbate layers (see below, Fig. 4).

The motivation for selecting these models comes from simulating experimentally realistic minimum configurations at both low and higher temperatures, including metastable geometries with one or more “O-down” CO molecules, which were observed experimentally post IR laser excitation of CO IS mode.<sup>9</sup>

## 2.2 *Ab initio* molecular dynamics

Starting from these models, AIMD simulations are performed within the canonical ensemble (NVT) using a Nosé–Hoover thermostat,<sup>24</sup> with the goal to arrive at vibrational spectra (see below). Initial velocities for AIMD are generated from Boltzmann distributions at  $T = 30$  K and  $T = 300$  K, respectively. We use the same supercells as for geometry optimization in AIMD for  $T = 30$  K, while for  $T = 300$  K the  $c$ -vector of the tetragonal unit cell was extended from 30 Å to 50 Å. Nuclear degrees of freedom are propagated with a time step of  $\Delta t = 0.5$  fs. The total simulation time for the low temperature (30 K) is 60–100 ps, that for the higher temperature (300 K) is 100 ps.

This was done by running several trajectories for each system, with equilibration and production phases, see the ESI,<sup>†</sup> Section S1.1 for details. There it is mentioned that for  $T = 300$  K, the protocol was slightly different compared to  $T = 30$  K: trajectories were first propagated in the NVT ensemble (as for  $T = 30$  K), but then propagated within the microcanonical ensemble (NVE) for another 5 ps to remove spurious effects caused by the thermostat coupling. For both temperatures, only the last segment of each trajectory was utilized to sample the correlation functions in an interval  $[0, t_{\text{sample}}]$ .  $t_{\text{sample}}$  determines the spectral resolution of vibrational spectra. If not stated otherwise, we choose  $t_{\text{sample}} = 3$  ps, leading to a resolution of  $\sim 11$   $\text{cm}^{-1}$ . This is larger than found in low-temperature experiments, which are typically less than 2  $\text{cm}^{-1}$  (ref. 8)–see also Section 3.4.2 below regarding this.

## 2.3 Methods for computing vibrational spectra

### 2.3.1 Normal mode analysis.

Normal mode analysis (NMA) is the simplest tool to model adsorbate vibrations from first principles, within the harmonic approximation and neglecting temperature effects and specific selection rules (and thus, intensities). In the NMAs reported below, the adsorbate molecules and top surface layer atoms are allowed to displace, using a step size of 0.02 Å. No frequency scaling has been applied. Additionally, IR intensities computed at the same level of theory (PBE+D2) are reported below; for more details on their computation see ESI,<sup>†</sup> Section S2.1.

### 2.3.2 Vibrational density of states (VDOS) from velocity–velocity autocorrelations functions (VVAFs).

At a next level towards spectra, vibrational density of states (VDOS) curves from Fourier transformed velocity–velocity autocorrelation functions (VVAFs) are calculated as:<sup>25,26</sup>

$$\text{VDOS}(\omega) \propto \sum_{i=1}^N \int_0^{\infty} \langle v_i(0) \cdot v_i(t) \rangle e^{-i\omega t} dt. \quad (1)$$



Here,  $\omega$  is the frequency,  $\mathbf{v}_i(t)$  the velocity of moving atom  $i$  at time  $t$  and  $N$  is the total number of moving atoms. CO molecules and the top NaCl layer atoms were allowed to move.  $\langle \mathbf{v}_i(0) \cdot \mathbf{v}_i(t) \rangle$  is the VVAF, averaged over different AIMD trajectories. To evaluate VVAFs, we use the so called “initial position method”<sup>26</sup> (see ESI,† Section S1). In practice, the time integral in eqn (1) is evaluated from 0 to  $t_{\text{sample}}$ , and the integrand is multiplied by a Hann window function  $w(t) = \cos^2(\pi t/(2t_{\text{sample}}))$  to avoid negative VDOS values.

Normally, the VDOS is evaluated based on velocities in Cartesian coordinates. To better identify the exact vibrational motion associated with a specific frequency, we report also the “internal VDOS”, wherein the internal motions (frustrated rotations, translations, *etc.*) are deconvoluted, providing a better assignment of the low-frequency modes.<sup>27</sup> In particular, we shall derive VDOS curves resolved w.r.t. to the six coordinates of a CO molecule relative to the surface, namely  $r$  (the C–O distance), the surface–molecule distance ( $Z$ ), the lateral center-of-mass positions ( $X$ ,  $Y$ ), and two angular coordinates, the polar ( $\theta$ ) and azimuthal ( $\phi$ ) angles. This is done numerically for each trajectory, by using “instantaneous” internal coordinates for each molecule, as outlined in the ESI,† Section S1.3. Also, molecule-wise decomposition of the simulated VDOS spectra will be shown and discussed below.

**2.3.3 IR absorption spectra from VVAFs.** We will also calculate infrared responses, related to the first-order susceptibility,  $\chi_{ab}^{(1)}$ . We concentrate on the IR response of the C–O stretch modes of CO/NaCl(100), where<sup>26</sup>

$$\chi_{ab}^{(1)}(\omega) = \frac{Q(\omega)\mu_{\text{CO}}'^2}{i\omega^2} \int_0^\infty \sum_i^M \sum_j^M \langle v_{b,j}^{\text{CO}}(0) \cdot v_{a,i}^{\text{CO}}(t) \rangle e^{-i\omega t} dt \quad (2)$$

with  $M$  C–O chromophores per cell. Here,  $Q(\omega)$  is a quantum correction factor, given by  $Q(\omega) = \hbar\omega/(k_{\text{B}}T(1 - \exp(-\hbar\omega/k_{\text{B}}T)))$  with  $k_{\text{B}}$  the Boltzmann constant. Further,  $v_{a,i}$  is the  $a$ -th component of the velocity vector of C–O bond  $i$ , and  $\mu'_{\text{CO}} = d\mu_{\text{CO}}/dr|_{\text{eq}}$  the dipole derivative of the CO chromophore along the C–O coordinate, at its equilibrium position,  $r = r_{\text{eq}}$ , assumed independent of  $\omega$  (Condon approximation). The parametrization of  $\mu'_{\text{CO}}$  is based on quantum chemistry calculations on the CAM-B3LYP+D3 level,<sup>28,29</sup> using the Gaussian program<sup>30</sup> and a cluster model with a CO upright on-top of NaCl(100), as outlined in the ESI,† Section S1.5, eqn (S6). These give a value of  $\mu'_{\text{CO}} = -0.8597e$ .

IR absorption spectra (for modes involving C–O stretches) are calculated from the imaginary part of  $\chi_{ab}^{(1)}$ . In particular, we will be interested in  $z$ -polarized IR spectra, for which the signal intensity is given as  $I_z^{\text{IR}}(\omega) \sim \text{Im} \chi_{zz}^{(1)}(\omega)$ .<sup>26</sup> In practice, the integral in eqn (2) is done again up to a finite time  $t_{\text{sample}}$ , and complemented by a Hann window function.

Another simplification of eqn (2), used also in ref. 25 and 26 is that, it assumes dipole moment derivatives being isotropic w.r.t. the surface. For CO/NaCl(100), this is not the case. Rather than re-deriving eqn (2) to include this dependence, we take the

anisotropy effect into account by a simplified procedure, leading, for the  $z$ -polarized case, to

$$\chi_{zz}^{(1)}(\omega) = \frac{Q(\omega)c'^2}{i\omega^2} \int_0^\infty \sum_i^M \langle \cos(\theta_i(0)) \cos(\theta_i(t)) \rangle \times \langle v_{z,i}^{\text{CO}}(0) \hat{r}_{z,i}(0) \cdot v_{z,i}^{\text{CO}}(t) \hat{r}_{z,i}(t) \rangle e^{-i\omega t} dt \quad (3)$$

where we take into account the dependence of  $\mu'_{\text{CO}}$  along  $z$  on the polar angle  $\theta$  (*cf.* ESI,† Section S1.5 and Fig. S3). Details concerning eqn (3) are described in the ESI,† Section S1.4, where also an expression (eqn (S3), ESI†) valid for  $x$ - and  $y$ -polarized spectra can be found, utilizing  $\theta$ -dependent  $\mu'_{\text{CO}}$  along  $x$  and  $y$ , respectively. In eqn (3),  $c'$  ( $= -0.899e$ ) is a parameter derived from fitting DFT results for a CO/NaCl cluster model of the dipole derivative to  $\frac{d\mu_z}{dr} = c' \cos(\theta)$ , *cf.* ESI,† Section S1.5. Further  $\hat{r}_{z,i}(t)$  is the  $z$ -component of the instantaneous unit CO bond vector for the  $i$ th CO molecule at time  $t$ . The form (3) is particularly relevant when computing integrated absorbance ratios of the IR response, especially at  $T = 300$  K (see below). We note that before taking the Fourier transform, one should normalize the molecularly decomposed VVAFs w.r.t. the absolute value of the total response, otherwise, the sign induced by so called “orientational” VVAFs would be washed away (see below).

**2.3.4 Vibrational sum frequency spectra from VVAFs.** Finally, vibrational sum frequency (VSF) spectra, which are particularly surface-sensitive are calculated *via* second-order susceptibility tensor elements,  $\chi_{abc}^{(2)}(\omega)$  (with  $a$ ,  $b$ ,  $c$  being Cartesian coordinates), from correlation functions. Rather than computing full VSF intensities, here we only take one of the tensor elements, *i.e.*,  $\chi_{xxz}^{(2)}$  ( $= \chi_{yyz}^{(2)}$ ), as a measure for VSF signals seen in an “ssp” polarization setup in experiments.<sup>26</sup> The second order susceptibility in terms of surface-specific VVAFs, involving C–O stretch vibrations, is given as<sup>25,26</sup>

$$\chi_{abc}^{(2)}(\omega) = \frac{Q(\omega)\mu'_{\text{CO}}\alpha'_{\text{CO}}}{i\omega^2} \int_0^\infty \sum_i^M \sum_j^M \left\langle v_{c,i}^{\text{CO}}(0) \frac{v_j^{\text{CO}}(t) r_j^{\text{CO}}(t)}{|r_j^{\text{CO}}(t)|} \right\rangle e^{-i\omega t} dt \quad (4)$$

if  $a = b$  and  $\chi_{abc}^{(2)}(\omega) = 0$  otherwise. Here,  $\alpha'_{\text{CO}}$  is the derivative of the  $ab$  component of polarizability of the C–O molecule along the C–O coordinate,  $r$ , and assumed independent of  $\omega$  again. They were either treated as constants or derived from linear fits of dipole derivatives of upright CO on NaCl along the molecular axis, and derivatives of  $\alpha_{xx}$ , respectively, using cluster models again (*cf.* ESI,† Section S1.5), giving  $\alpha'_{xx} = 3.49a_0^2$ . Total VSF intensities are computed as  $I_{\text{ssp}}^{\text{VSF}} \propto |\chi_{xxz}^{(2)}(\omega)|^2$  in this work, while real and imaginary parts of  $\chi_{xxz}^{(2)}(\omega)$  serve to be useful for understanding orientational effects.

Again, the above formulation does not account for anisotropies of the polarizability derivatives, and also not of the dipole derivatives. Following a similar approach as done for the 1st order susceptibility, we modify the original VSF response<sup>25</sup> by



including the angular dependence of the dipole and polarizability derivatives as, for the “ssp” (or “xxz”) case:

$$\chi_{xxz}^{(2)}(\omega) = \frac{Q(\omega)c'd'}{i\omega^2} \int_0^\infty \sum_i^M \langle \cos(\theta_i(0))(\cos(b'\theta_i(t) + e') + d') \rangle \times \left\langle v_{z,i}^{\text{CO}}(0) \hat{r}_{z,i}^{\text{CO}}(0) \frac{v_i^{\text{CO}}(t) L_i^{\text{CO}}(t)}{|L_i^{\text{CO}}(t)|} \right\rangle e^{-i\omega t} dt \quad (5)$$

For the polarizability derivative  $\alpha'_{\text{CO}}$  in eqn (4) we take specifically for the “ssp” polarized response the  $\alpha_{xx}$  derivative, which then leads to eqn (5). The  $a'$ ,  $b'$ ,  $e'$  and  $d'$  are parameters, again based on cluster models (see ESI,† Section S1.5), and a fit  $d\alpha_{xx}/dr = a' \cos(b'\theta + e') + d'$ , with  $a' = 2.99$ ,  $b' = 1.55$ ,  $e' = -2.146$  and  $d' = 5.62$  (all in atomic units, except  $b'$ , which is a constant and  $e'$  which is in rad.) The parameter  $c'$  is the same as before.

**2.3.5 Intermolecular couplings in vibrational spectra: cross-correlations.** So far we have only considered autocorrelation terms into the formulations given in eqn (3) and (5). Including cross correlation terms, in addition to the autocorrelation terms, into the above expressions of the 1st and 2nd order susceptibility brings us closer to modelling real spectra by going beyond the dilute coverage limit and taking neighbouring intermolecular interactions into account. Instead of taking a radial cutoff function, as done by Ohto *et al.* in their work,<sup>25</sup> we define a cross coupling coefficient constant,  $g(i,j)$ , which introduces, for  $g(i,j) \neq 0$ , where  $i \neq j$ , cross-correlations between the individual CO molecules,  $i$  and  $j$ , leading to modifications of eqn (3) and (5) as follows:

$$\chi_{zz}^{(1)}(\omega) = \frac{Q(\omega)c'^2}{i\omega^2} \int_0^\infty \sum_i^M \sum_j^M \langle g(i,j) \cos(\theta_j(0)) \cos(\theta_i(t)) \rangle \times v_{z,j}^{\text{CO}}(0) \hat{r}_{z,j}^{\text{CO}}(0) \cdot v_{z,i}^{\text{CO}}(t) \hat{r}_{z,i}^{\text{CO}}(t) \rangle e^{-i\omega t} dt \quad (6)$$

$$\chi_{xxz}^{(2)}(\omega) = \frac{Q(\omega)c'd'}{i\omega^2} \int_0^\infty \sum_i^M \sum_j^M \langle g(i,j) \cos(\theta_i(0)) (\cos(b'\theta_j(t) + e') + d') \rangle \times v_{z,i}^{\text{CO}}(0) \hat{r}_{z,i}^{\text{CO}}(0) \frac{v_j^{\text{CO}}(t) L_j^{\text{CO}}(t)}{|L_j^{\text{CO}}(t)|} \rangle e^{-i\omega t} dt. \quad (7)$$

We set  $g(i,j) = 1$  in our case, in order to correlate all CO molecules. A pictorial summary of the AIMD approach to VDOS, IR and VSF spectra calculations used in this work is shown in the ESI,† Section S1.6 and Fig. S4.

## 2.4 Analysis of internal mode correlations

We quantify internal mode correlations not only from spectra but also from AIMD trajectories. First, angular and CO-surface distance distribution probabilities are calculated as

$$P(a) = \frac{n_a}{N_t} \quad (8)$$

with  $a = \theta$ ,  $\phi$ , and  $Z$ . Here,  $n_a$  is the number of time steps associated with a certain value of coordinate  $a$ , and  $N_t$  is the total number of time steps. A bin width of  $10^\circ$  is chosen for  $\theta$  and  $\phi$ , and  $0.05 \text{ \AA}$  for  $Z$ . In order to check for angular correlations between the angular internal DoFs of the individual CO molecules,  $\{\theta, \phi\}$ , we evaluate joint distribution probabilities,  $P(\theta, \phi)$  and compare them with the product  $P(\theta) \cdot P(\phi)$ . If not the same, both angles are correlated.

In a more generalized approach, correlation between all internal DoFs can be measured *via* correlation coefficients. Below we shall occasionally study so-called distance correlation matrices (as defined by Székely *et al.*<sup>31</sup>), where covariances of the quantities themselves are evaluated not from their respective means, but from distances of all other points. We evaluate intra- and inter-correlation distance matrices with elements  $R(a,b)$ , which indicate the correlation of internal DoF  $a \in \{r, \theta, \phi, X, Y, Z\}$  of a CO molecule with internal DoF  $b$  of the same or another molecule. The mathematical definition of the distance correlation matrices used in this work is given in the ESI,† Section S4.3.

## 3 Results and discussion

### 3.1 Energetics of different phases

On the PBE+D2 level of theory, for monolayer structures (C, D, E and F in Fig. 2), the “all C-bound” P/U 1 ML structure D is 20 meV ( $\sim 161 \text{ cm}^{-1}$ ) higher in energy per CO compared to the “all C-bound” 1 ML T/A configuration, D. The latter is the most stable structure found (*cf.* Table 1). The T/A configurations with one “O-bound” CO per cell (structure E), is 84 meV ( $\sim 678 \text{ cm}^{-1}$ ) higher in energy than D, which is the energy needed to flip one CO from “C-bound” to “O-bound” while keeping the neighbouring COs “C-bound”. Flipping all (four) “C-bound” COs to “O-bound” (structure F), costs 85 meV ( $\sim 686 \text{ cm}^{-1}$ ) per CO molecule, showing that the C-bound  $\rightarrow$  O-bound flipping energy is largely independent of the orientation of CO neighbours. For completeness, we note that the classical isomerization barrier for the back-flipping reaction (O-bound  $\rightarrow$  C-bound) is  $\sim 500 \text{ cm}^{-1}$  in a 1/8 ML coverage compared to  $\sim 570 \text{ cm}^{-1}$  for a 1/4 ML coverage.<sup>16</sup> For monolayer and buried monolayer cases, computed minimum energy pathways indicate isomerization barriers near 565 and  $600 \text{ cm}^{-1}$  respectively,<sup>13</sup> reflecting a dependence of CO coverage on the isomerization barrier.

We also computed Gibbs free energies,  $G = H - TS = E_{\text{SCF}} + G_{\text{vib}}$  (with  $H$  being the enthalpy and  $S$  the entropy), taking vibrations in harmonic approximation from normal mode analysis into account,<sup>32</sup> *cf.* Section 3.2. The free energy contains, in addition to SCF energies  $E_{\text{SCF}}$ , zero-point energy, finite- $T$  vibrational enthalpy contributions and also vibrational entropies (summarized in  $G_{\text{vib}}$ ). Within the harmonic approximation, we find that the T/A all “C-bound” phase remains the most stable phase for temperatures up to 150 K, *i.e.*, in particular no T/A  $\rightarrow$  P/U phase transition (expected around 35 K) is found, *cf.* ESI,† Section S2.2. The harmonic approximation and the utilized DFT



**Table 1** PBE+D2 energies (relative to the most stable phase, C), and CO stretch normal mode frequencies for 1 ML phases of CO/NaCl(100), at optimized geometries (see Fig. 2). The last four columns correspond to normal mode (CO-stretch) frequencies of the individual CO adsorbates in the unit cell. The IR intensities (normalized w.r.t. the highest intensity peak found in each structure), as described in ESI, Section S2 are reported in brackets for each normal mode. Note that the intensities are to be considered approximate as they are derived from periodic calculations and are highly sensitive to the harmonic frequencies, which depend upon the specified parameters such as energy convergence threshold,  $k$ -point grid, displacement step, etc., in the NMA. Additionally note that surface atoms were also displaced along with the CO(s) in the NMA. For frequencies, the low-coverage model A is shown for comparison

Configuration	Energy/CO (meV)	C–O stretch frequencies ( $\text{cm}^{-1}$ )			
A (1/4 ML, “C-bound”)	—	2141.2	—	—	—
B (1/2 ML, “C-bound”)	—	2128.2 (1.0000)	2122.7 (0.0763)	—	—
C (T/A, “all C-bound”)	0	2128.5 (1.0000)	2124.2 (0.1738)	2121.6 (0.0193)	2119.5 (0.0296)
D (P/U, “all C-bound”)	20	2138.6 (1.0000)	2131.1 (0.0729)	2127.4 (0.0402)	2119.3 (0.0041)
E (T/A, “one O-bound”)	84	2127.6 (1.0000)	2122.6 (0.0011)	2120.9 (0.0432)	2116.2 (0.0146)
F (T/A, “all O-bound”)	85	2121.3 (0.0596)	2120.9 (0.2314)	2118.2 (1.0000)	2109.0 (0.0174)

functional (owing to the presence of small imaginary frequencies for the P/U phase) is found to be insufficient to show such an effect.

### 3.2 “Vibrational spectra” from normal mode analysis

NMA gives a first idea on vibrational spectra. The harmonic C–O stretch frequencies for the 1 ML phases C–F are also listed in Table 1, as well as the CO frequency of the low-coverage model A for comparison. Further, in the ESI,<sup>†</sup> Section S2.1 and Fig. S5 we show normal mode “spectra”, obtained from Gaussian broadening of stick spectra for optimized configurations A–F of CO/NaCl(100). (Also, some technical details of NMAs are described in the ESI.<sup>†</sup>)

For the tilted/antiparallel (T/A) phase of the CO monolayer on NaCl(100), the fundamental C–O stretch mode yields vibrational frequencies in the range 2120–2130  $\text{cm}^{-1}$ , for different combinations of in-phase and out-of-phase vibrations for the four adsorbed CO molecules. For the lowest coverage studied, *i.e.*, 0.25 ML (model A), the C–O stretch mode is blue-shifted peaking at  $\sim 2141 \text{ cm}^{-1}$ . The 1 ML P/U phase (model D) of CO/NaCl(100) shows frequencies between 2138–2119  $\text{cm}^{-1}$  in the C–O stretch region, a broader frequency range compared to the T/A phase (model C). For the remaining metastable 1 ML T/A configurations with one (model E) or more “O-down” CO molecules (model F), we see frequencies in the range 2109–2128  $\text{cm}^{-1}$ . Comparing to experimental results in ref. 9, we see a systematic red-shift of the PBE+D2 NMA frequencies by  $\sim 20 \text{ cm}^{-1}$ .

In summary, for the 1 ML T/A phases, flipping one or all CO molecules to “O-down” leads (i) to a broader frequency range, and (ii) to an overall red-shift of (some parts of) the spectrum. We further see that (iii) the frequency of low-coverage CO/NaCl(100) (model A) is blue-shifted w.r.t. the highest-energy peak of all T/A ML phases, by at least  $10 \text{ cm}^{-1}$ .

In addition to the high-frequency modes, CO frustrated bending and CO–surface modes for the “C-bound” configurations are found, with frequencies around 100–160  $\text{cm}^{-1}$  and 70–100  $\text{cm}^{-1}$ , respectively. Below 60  $\text{cm}^{-1}$ , we mainly find CO librational modes. The substrate phonons span over the frequency region between 0–220  $\text{cm}^{-1}$ .

### 3.3 Vibrational density of states and AIMD analysis

To go beyond harmonic and zero-temperature approximations, VDOS curves were calculated from AIMD at two temperatures,

$T = 30$  and  $300 \text{ K}$ . The latter corresponding to room temperature was chosen to study (plausible) thermally-induced CO flipping in the system and its influence on the different vibrational spectra simulated below. The AIMD simulations also serve to provide insight into the ongoing dynamics.

#### 3.3.1 VDOS and dynamics at low temperature: $T = 30 \text{ K}$ .

In Fig. 3, we report VDOS curves for three coverages of CO/NaCl, 0.25 (model A), 0.5 (B) and 1 ML T/A phase with all “C-bound” (model C). The total VDOS is also decomposed into different subsystems, of individual CO molecules and the NaCl surface. For the monolayer coverage, the CO internal stretch vibrations are found to be centered around  $\sim 2125 \text{ cm}^{-1}$  (dashed vertical line), which is comparable to the harmonic frequencies obtained from NMA (Table 1). With decreasing coverages, the CO stretch peak maxima blue-shift towards higher wavenumbers, which is concordant with experiments<sup>5</sup> and the NMA. For instance, for 0.25 ML coverage the CO stretch signal blue-shifts by  $\sim 9 \text{ cm}^{-1}$  w.r.t. to the 1 ML case. Note, however, that the NMA frequency for the CO stretch at this coverage is blue-shifted by  $7 \text{ cm}^{-1}$  w.r.t. the VDOS frequency. This can be attributed to anharmonicity effects as well as sampling of orientationally varied (tilted) configurations at 30 K compared to NMA. Additionally note that the anharmonicity constant derived from experiments<sup>9</sup> for the C-bound monolayer is  $13.35 \text{ cm}^{-1}$ . However, a direct comparison with the present results cannot be drawn at the moment.

Before considering low-frequency modes which are also shown in Fig. 3 (left), we discuss the effects of flipping one or several CO molecules “upside down” and of additional CO layers on CO stretch frequencies in Fig. 4. There we report the VDOS curves for 1 ML T/A models with one “O-bound” CO (model E), and all “O-bound” CO configurations (model F). In addition, the already mentioned, new (PBE+D2 optimized) model G is shown, with a CO-buried monolayer with one “O-bound” CO (see also ref. 13).

The VDOS curve for model E shows a broader peak in the CO-stretch region, with the “O-bound” signal around  $2116 \text{ cm}^{-1}$ , red-shifted from the “C-bound” CO signals around  $2125 \text{ cm}^{-1}$  (see also model C, and dashed vertical line). The red-shift of about  $9 \text{ cm}^{-1}$  is somewhat lower than the shift of  $\sim 15 \text{ cm}^{-1}$  found experimentally in ref. 9, albeit for a 1 ML  $^{13}\text{C}^{18}\text{O}/\text{NaCl}(100)$  system. The VDOS of the buried model G has a higher VDOS



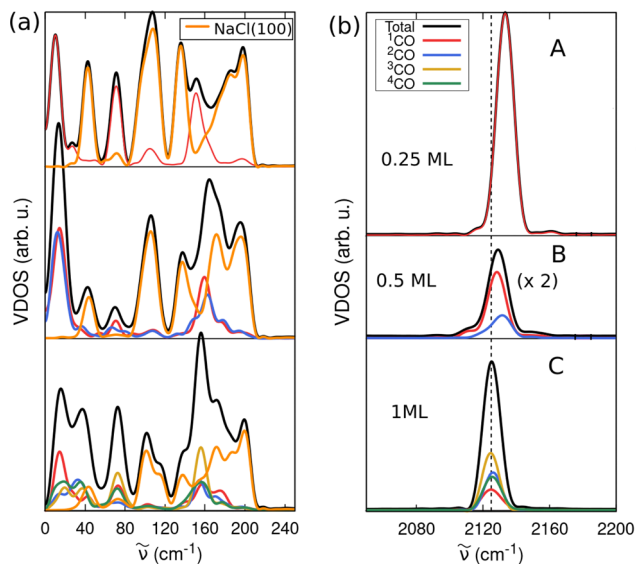


**Fig. 3** VDOS curves for “C-bound” phases of CO/NaCl(100) at coverages 0.25 (model A), 0.5 ML (model B), and 1 ML (T/A, model C), all at 30 K. Left panels (a) show the low-frequency region and right ones (b) the C–O stretch region. Total VDOS in black, NaCl VDOS in orange, other colors indicate CO VDOSs. The vertical line on the right indicates the main C–O stretch frequency of model C, highlighting a blue-shift of the signal at lower coverages.

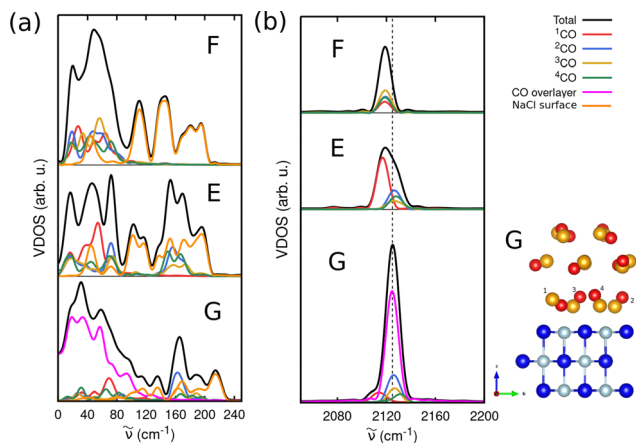


**Fig. 4** VDOS curves for 1 ML T/A phases of CO/NaCl(100) with all “O-down” (model F), one “O-down” (E), and the “buried monolayer” with one “O-down”, and two CO overlayers (model G, optimized structure on the right), obtained from AIMD at 30 K. Left panels (a) show the low-frequency region, right ones (b) the C–O stretch region. Total VDOS in black, NaCl VDOS in orange, other colours are CO VDOSs. The vertical line on the right indicates the main C–O stretch frequency of model C, indicating a red-shift for “O-down” configurations.

intensity in the C–O stretch region compared to model E, due to the contributions of the CO overlayers. (The same VDOS scale has been used in the three panels F, E, G.) When finally going to model F (no overlayers, all four CO molecules “O-down”), all C–O stretch vibrations are red-shifted w.r.t. “C-down”, in agreement with experiments<sup>9</sup> and the NMA (see Table 1).

For the T/A monolayer phases, at  $T = 30$  K, AIMD predict for “C-down” configurations narrow  $\theta$  distributions with a mean around  $30^\circ$  over the sampling time of the canonical trajectories (*cf.* ESI,<sup>†</sup> Section S4.1 and Fig. S11(a)), along with a moderate lateral displacement of COs away from  $\text{Na}^+$ , by  $< 1$  Å (not shown). “O-bound” CO have a mean, averaged angular probability distribution  $P(\theta)$  of  $130^\circ$  ( $50^\circ$  w.r.t. the axis perpendicular to the surface), *cf.* Fig. S11(b) and (c) (ESI<sup>†</sup>), and show more lateral translation compared to the “C-bound” CO molecules, by up to  $\sim 1.7$  Å away from  $\text{Na}^+$  (not shown). In all cases, the long-range T/A order is largely maintained in the monolayer configurations. We further note that during the timescale of our simulations ( $\sim 3 \times 30$  ps), none of the “O-bound” CO molecules flipped to “C-down” in the monolayer case. In contrast, for a low-coverage case (0.25 ML) in an “O-bound” configuration, we found, in a single test trajectory, CO flipping to the more stable “C-bound” at 22 K within 10 ps (not shown here). This indicates that the presence of neighbouring COs provides new channels for energy transfer and therefore may decrease the flipping rate relative to low coverages. Note that in experiment,<sup>12</sup> at around  $T = 20$  K, “O-down”  $^{12}\text{C}^{16}\text{O}$  molecules in buried monolayers on NaCl, flip with a rate of  $\sim 10^{-4}$  s $^{-1}$ , indicating a flipping time of several hours.

Turning now our focus to the low-frequency region of the VDOS curves in Fig. 3 and 4, we find it to be dominated by CO-surface vibrations and CO frustrated translations (tangential motion along the surface) and rotations, as well as phonon modes from the NaCl surface, up to  $200$  cm $^{-1}$ . We can more unambiguously assign internal motions responsible for respective peaks by inspecting the internally resolved VDOS as defined in the ESI,<sup>†</sup> Section S1.3. For instance, in Fig. 5(a), we observe that the frustrated  $\theta$  rotation contributes to peaks observed at  $\sim 150, 180$  cm $^{-1}$  and a minor peak around  $40$  cm $^{-1}$ . Peaks associated with frustrated translations appear at frequencies below  $45$  cm $^{-1}$ . The predominant peak at  $160$  cm $^{-1}$  arises from the frustrated azimuthal angle ( $\phi$ ) rotation, with additional contributions around  $90$  and  $30$  cm $^{-1}$ . Motion perpendicular to the CO-surface ( $Z$ ) results in peaks at around  $75, 165,$  and  $205$  cm $^{-1}$ . Comparing the Cartesian and internal VDOSs, we note that in the low-frequency region ( $0$ – $140$  cm $^{-1}$ ), the latter is smaller than the former, compensated by the larger peak at  $160$  cm $^{-1}$  from the frustrated  $\phi$  motion. The enhanced low-frequency normal modes are speculated to stem from coupling between the internal  $\phi$  motion and other librational modes. Note that the total integrated area under the Cartesian and internal VDOS is the same. Interestingly, for “O-bound” CO adsorbates (Fig. 5(b)), all the low frequency modes are also largely red-shifted compared to the vibrations coming from the “C-bound” adsorbates. Note here that the PBE+D2 values for the low-frequency region may lack accuracy due to the dominance of dispersion effects and the incomplete cancellation of self-interaction errors in the applied DFT method. As such, the reported values should be regarded as approximate.

**3.3.2 VDOS and dynamics at higher temperature:  $T = 300$  K.** To study vibrational dynamics at a higher temperature,  $T = 300$  K, we chose the monolayer P/U phase with all CO



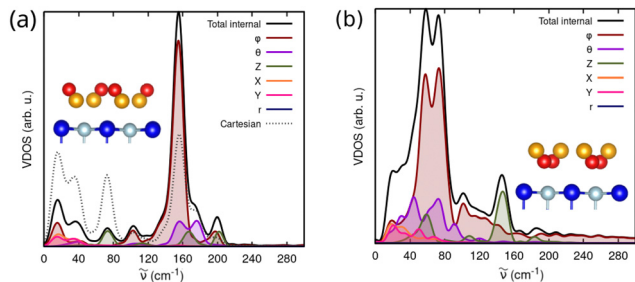


Fig. 5 Internal VDOS in the low frequency regime for motions along  $X$ ,  $Y$ ,  $Z$ ,  $\theta$ ,  $\phi$  and  $r$  for a monolayer (a) with all “C-bound” CO (model C) and (b) with all “O-bound” CO (model F) on NaCl(100), all at 30 K. The Cartesian VDOSs are shown for comparison.

“C down” (model D in Fig. 2) and the T/A ML phase with one “O-bound” CO (model E in Fig. 2) as starting points. Recall from above and from the ESI,<sup>†</sup> Section S1.1, that a slightly different protocol compared to  $T = 30$  K was used. We ran NVT trajectories to equilibrate the respective configurations at  $T = 300$  K and at this temperature, within the timescale of 20 ps, CO adsorbates underwent desorption in a sequential fashion. Therefore, in every trajectory run, varying coverages of CO were obtained. Removing the already desorbed molecules which surpassed a dividing plane 15 Å above the NaCl surface, we progressed with the simulations in the microcanonical ensemble to remove thermostat effects. Since every trajectory contains also “quasi-desorbed” molecules that are still close ( $< 15$  Å above) the NaCl surface, we expect rovibrational signatures in our spectra due to these “quasi-free” molecules. The VDOS curves reported here have been extracted from the last segment of such NVE-AIMD trajectories ( $t_{\text{sample}} = 3$  ps).

In Fig. 6 we show Cartesian and internal VDOS curves for both studied systems, in low- and high-frequency (C–O stretch) regimes. Also shown are trajectory snapshots for both systems, indicating large-amplitude motions away from the surface and

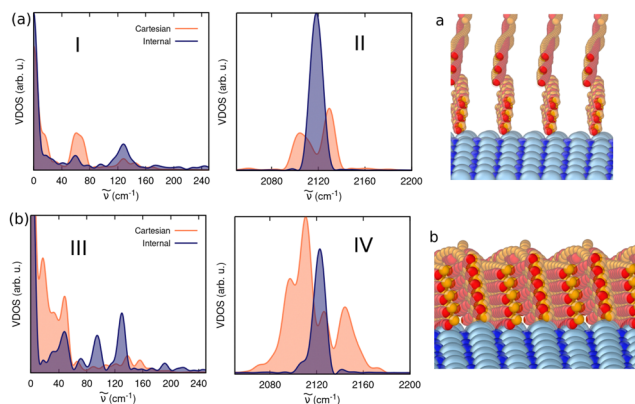


Fig. 6 Cartesian and internal VDOS of (a) 1 ML P/U phase of CO/NaCl(100) (model D, panels (I) and (II)) and (b) 1 ML T/A phase CO/NaCl(100) with one “O-down” CO (model E, panels (III) and (IV)), all after equilibration at 300 K and subsequent NVE-AIMD (see text). Low-frequency (I) and (III) and high-frequency regimes (II) and (IV) are shown. Trajectory snapshots are shown for the respective cases, indicating large-amplitude perpendicular motions.

even desorption. In general, the VDOS profile is broader compared to the  $T = 30$  K spectra. (As expected, also angular distributions  $P(\theta)$  and  $P(\phi)$  are much broader at  $T = 300$  K compared to  $T = 30$  K, cf. Fig. S12 in the ESI,<sup>†</sup> Section S4.1.) One can discern from Fig. 6(II), that the Cartesian VDOS (orange curve) obtained for the 1 ML P/U phase starting configuration shows a doublet peak around 2110  $\text{cm}^{-1}$  and 2138  $\text{cm}^{-1}$  resulting from rovibrational coupling typically observed for gas-phase CO spectra: the two peaks correspond to two rotational transition branches, R ( $J \rightarrow J + 1$ ; blue-shifted) and P ( $J \rightarrow J - 1$ ; red-shifted), the dip in the middle signifying the vibrational transition from  $\nu \rightarrow 0$  to  $\nu \rightarrow 1$ . For the internal VDOS (blue), the ro-vibrational structure disappears due to the elimination of the velocity component responsible for the CO bond rotation, and only a single peak appears at  $\sim 2125$   $\text{cm}^{-1}$ . Upon closer examination, one can also observe oscillations in the total internal VDOS spectra in the CO stretch regime. These stem from the azimuthal DoFs of the pseudo gas-phase CO molecules present above the NaCl surface which undergo rapid azimuthal motion, flipping, “roaming” and desorption of the CO molecules. Insight into large-amplitude motions along  $Z$ , for example, at high  $T$ , can be gained from CO–surface distance probability distributions  $P(Z)$  in the ESI,<sup>†</sup> Section S4.2 and Fig. S13, highlighting also that desorption is negligible at  $T = 30$  K. For the case where initial configuration at equilibrium was one “O-bound” CO surrounded by “C-bound” COs, similar flipping and desorption events are observed. In some trajectories the CO adsorbates are far above the surface and undergo periodic flipping, with a time period of  $\sim 0.7$  ps. In the Cartesian VDOS reported in Fig. 6(IV), we find quartet peaks spanning the CO-stretch stretch region, while only one peak with a shoulder appears in the internal VDOS. This showcases more complex dynamics due to the initial presence of differently oriented CO molecules. Note here, a recent study by Nandi *et al.*,<sup>33</sup> which reported roaming-facilitated isomerization dynamics in the same system, albeit at low temperatures, using quasi-classical trajectories and cluster models.

The low-frequency VDOS curves at  $T = 300$  K (panels I, III) are qualitatively similar to those found at  $T = 30$  K, the main difference being larger relative weights in lowest-energy regions at and below  $\sim 50$   $\text{cm}^{-1}$ . Again, this is a consequence of internal rotation diffusion,<sup>27</sup> *i.e.*, less hindered translational and rotational motions of some molecules at the higher temperature.

**3.3.3 (Further) analysis of AIMD trajectories.** From all of these observations, we conclude that at most submonolayer coverages are probable to exist at room temperature, with pseudo gas-phase CO residing in the vicinity above the surface. We note, in fact, that there is no coverage of CO on NaCl(100) observed at room temperatures in experiments, which would be consistent with our simulations when extended to larger timescales beyond several picoseconds. At 300 K, the (low frequency) internal DoFs of CO molecules on the surface are also highly correlated, both within one molecule and between molecules. As an example, in Fig. 7 we illustrate angular ( $\theta$ ,  $\phi$ ), intramolecular joint and product probability curves (upper and



lower panels, respectively), for the case of a 1 ML P/U starting configuration (model D). Shown are product probabilities  $P(\theta)$ ,  $P(\phi)$  and joint probabilities  $P(\theta, \phi)$  (cf. Section 2.4).

A clear difference can be seen between them in Fig. 7(a), where the joint probability distribution curve manifests a double-stranded structure in contrast to the product probability curve which displays a lack of structure and a wide distribution over  $\{\theta, \phi\}$ . The fact that  $P(\theta, \phi) \neq P(\theta)P(\phi)$  signifies a correlation between the angular degrees of freedom, near room temperature where enough thermal energy for vibrational excitation of the angular modes is available. Also, flipping events manifest as “S-type” curves in the joint probability functions, signifying correlated  $(\theta, \phi)$  motion.

In order to go beyond angular correlations, we evaluated distance correlation matrices for all internal DoFs as described in Section 2.4 and ESI,† Section S4.3. Selected intra- and intermolecular correlation matrices with elements  $R(a, b)$  are reported in the ESI,† Section S4.3 (Fig. S14–S16), for various coverages and models. As only one finding we mention here that the internal C–O stretch mode ( $r$ ), largely independent of model, is typically decoupled from all other modes, both within a molecule and between two CO molecules. In contrast, angular and translational DoFs are more strongly coupled among each other. Further details, also regarding “O-down” vs. “C-down” configurations, are provided in the ESI.†

We also studied diffusion and orientational dynamics of the disordered CO adsorbates at 300 K, more details can be found in ESI,† Section S4.4.

### 3.4 Infrared spectra

**3.4.1 IR spectra and absorbance ratios at  $T = 30$  K.** VDOS curves are useful but cannot directly be connected to experimental spectra, e.g., their intensities and polarization

dependences. In order to make a more direct contact to experiment, we note that recent experimental investigations of CO/NaCl,<sup>8</sup> have concentrated on the integrated absorbance ratio (IAR),  $A_s/A_p$ , the ratio of the integrated area under an “s-polarized” absorption spectrum and the integrated area under a “p-polarized” absorption spectrum. Here, we compute IARs as a ratio of first-order susceptibilities evaluated along parallel and perpendicular directions w.r.t. the surface, i.e.,

$$\frac{A_s}{A_p} = \frac{\int_0^\infty (\text{Im}\{\chi_{xx}^{(1)}\} + \text{Im}\{\chi_{yy}^{(1)}\}) d\omega}{\int_0^\infty \text{Im}\{\chi_{zz}^{(1)}\} d\omega}. \quad (9)$$

Experimental IARs for low coverages (“C-bound” configurations) at 10 K were found to be very small, however, increasing abruptly at coverages close to 0.2 ML, followed by a gradual further increase up to 1 ML, where IAR was 0.28.<sup>8</sup> This observation suggested a transition from predominantly parallel CO orientations, to tilt geometries, when coverages approach 0.2 ML. In general, the IAR is expected to vary with coverage, temperature, and adsorbate orientations (e.g., “C-down” vs. “O-down”). This section provides an insight into how these factors influence the spectra simulated for all configurations of CO/NaCl(100) in Fig. 2.

The parametrized formulation (3) for  $\chi_{ab}^{(1)}(\omega)$  with ACFs (with orientation factors) has been utilized to simulate the IR responses if not stated otherwise. A comparison with the original formulation (2) without angle-dependent dipole derivatives, can be found in the ESI,† Section S3.1 and Fig. S7, for the  $T = 300$  K case. As argued there, in particular at these higher temperatures when CO molecules undergo large-amplitude motions, eqn (3) (and eqn (S3), ESI†) is expected to be the more accurate approach – more evidence will be given shortly.

Fig. 8 shows IR spectral responses at  $T = 30$  K, for two low-coverage models of 0.25 ML and 0.5 ML (model A and B in

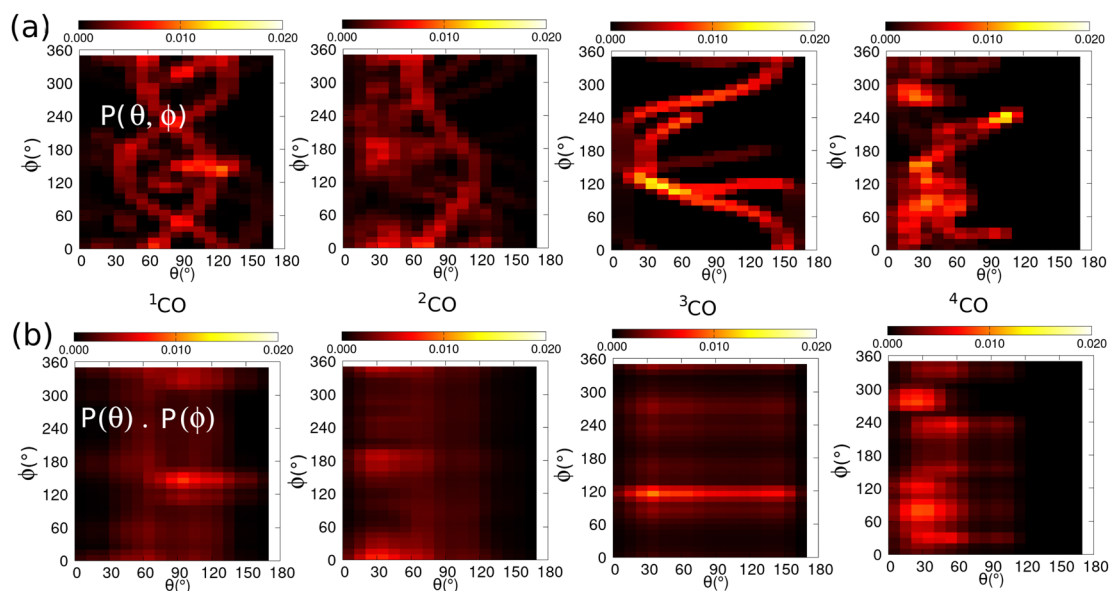


Fig. 7 Averaged (over five trajectories), (a) intramolecular joint and (b) product probability distributions of angular DoFs,  $\theta$  and  $\phi$ , for CO adsorbates  $^1\text{CO}$  to  $^4\text{CO}$  (from left to right), during the last phase (for 3 ps) of NVE runs after equilibration at 300 K, for the 1 ML P/U model (model D).



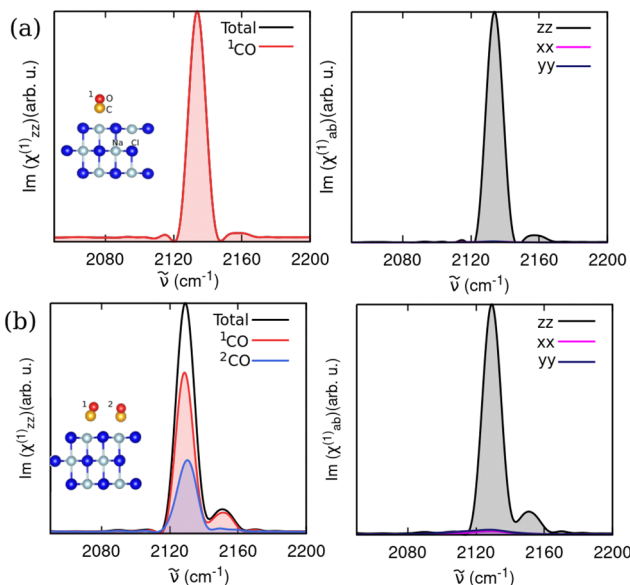


Fig. 8 Computed IR spectral response of CO/NaCl(100) from trajectories starting from (a) 0.25 ML (model A), (b) 0.5 ML (model B) all “C-bound” configurations equilibrated at 30 K. Averages over three trajectories are shown, and molecule-wise and polarization dependences are indicated as well.

Fig. 2). For 0.25 ML (Fig. 8(a)), the peak maximum is found around  $2134\text{ cm}^{-1}$ , blue-shifted compared to the 0.5 ML case (Fig. 8(b)), where the CO-stretch peak occurs at  $2128\text{ cm}^{-1}$ . The overall red-shift with increasing coverage is consistent with the VDOS curves reported earlier. Experimentally, FTIR absorption peaks for CO/NaCl at 0.57 ML, for example, at 10 K, are at

around  $2155\text{ cm}^{-1}$ ,<sup>8</sup> reflecting a systematic red-shift of the PBE+D2 AIMD frequencies by  $\sim 30\text{ cm}^{-1}$ . Note that the width of the IR spectra reported here arises not only from thermal effects but also from the limited propagation time of the AIMD simulations yielding a resolution of  $11\text{ cm}^{-1}$ , as mentioned before.

From the simulated polarization-dependent spectra at both coverages, we observe much weaker *x*- and *y*-polarized responses compared to the *z*-polarized response. The IAR is 0.01 and 0.07 for 0.25 and 0.5 ML coverages, respectively. The IARs are 0.06 and 0.1 when evaluated using the original formulation for the  $\chi_{ab}^{(1)}$  in eqn (2), showing that the anisotropy of the dipole moment derivative causes smaller IARs, even at the low temperature of 30 K. Experiments<sup>8</sup> give IARs for a 0.25 and 0.5 ML CO/NaCl(100) sample at 10 K of  $<0.05$  and  $<0.15$ , respectively. Thus we obtain the same trend, however, due to different temperatures ( $T = 10\text{ K}$  in experiment, 30 K in simulation), a quantitative agreement cannot be expected.

We then computed analogous spectra in the CO-stretch region for 1 ML T/A CO/NaCl(100) equilibrated at 30 K for different CO orientations, namely all “C-bound” (model C), one “O-bound” (model E) and all “O-bound” (model F) in Fig. 9. For the all “C-bound” configuration (Fig. 9(a)), a Lorentz-like band profile is observed with a single broad peak at  $\sim 2125\text{ cm}^{-1}$ . The one “O-bound” configuration (Fig. 9(b)), results in a broader peak, due to the presence of the red-shifted peak around  $2117\text{ cm}^{-1}$  originating from the “O-bound” CO, similar to the VDOS curves. The all “O-bound” configuration (Fig. 9(c)), yields a peak maximum around  $2118\text{ cm}^{-1}$ . The computed IARs are 0.08, 0.33 and 0.38 for the all “C-bound”, one “O-bound” and all “O-bound” configurations, respectively, showing that the CO orientation (“C-down” vs. “O-down”) has a substantial effect on IARs.

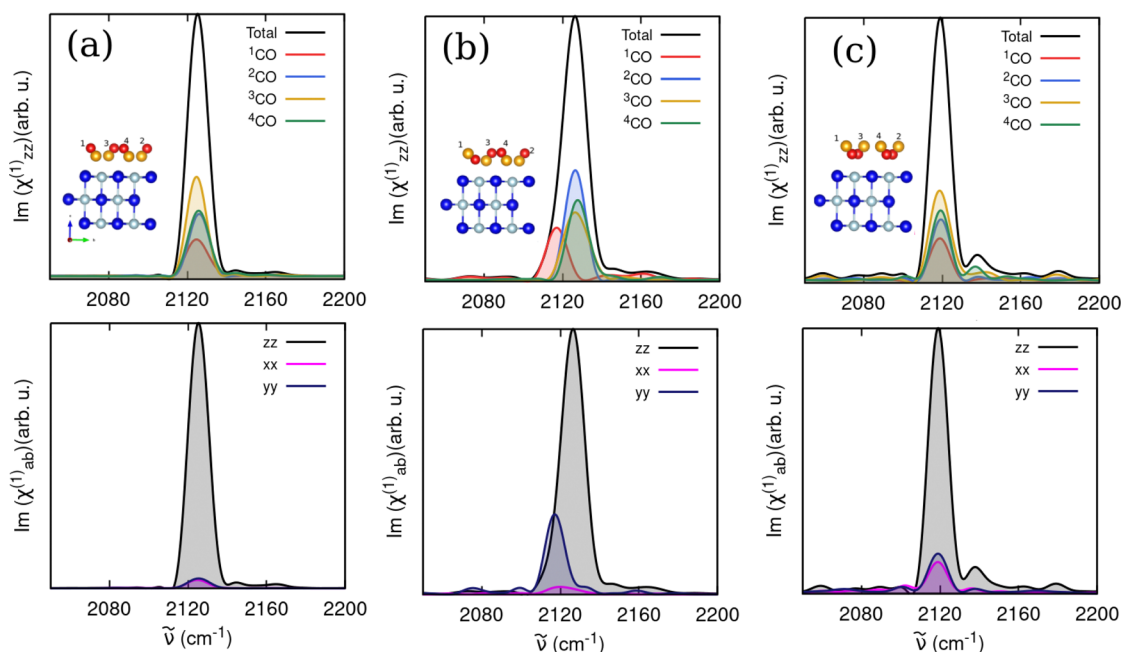


Fig. 9 Computed IR spectral response of CO/NaCl(100) from trajectories starting from 1 ML T/A phases (a) all “C-bound” (model C), (b) one “O-bound” (model E), (c) all “O-bound” (model F), all equilibrated at 30 K. Averages over three trajectories are shown, and molecule-wise and polarization dependences are indicated as well.



We also investigated the effect of intermolecular couplings by including velocity cross-correlation functions among the different CO adsorbates in the first-order susceptibility expressions (eqn (6)). As shown in the ESI,<sup>†</sup> Section S3.2, for the 1 ML system with one “O down” (model E) at 30 K, the inclusion of cross-correlation influences spectra of all molecules by blue-shifting the C–O peaks by a few wavenumbers ( $\sim 4 \text{ cm}^{-1}$ ), and changing their relative intensities. In this case, IAR values are only moderately increased, from 0.33 without cross-terms to 0.38 with cross-terms. Further discussions on the role of cross-correlations on the IR spectral response can be found in the ESI,<sup>†</sup> Section S3.2.

**3.4.2 IR spectra near room temperature:  $T = 300 \text{ K}$ .** Next, we computed room-temperature IR spectra for 1 ML configurations D (P/U) and E (T/A, one “O-down”) in Fig. 10. The spectra shown there are broader than the low-temperature spectra (Fig. 9) capturing thermal effects, with branched spectral features between  $[2060, 2190] \text{ cm}^{-1}$ . Note that the spectra are also characterized by sub-monolayer coverages persistent at 300 K for both starting configurations due to partial desorption and the occurrence of pseudo-gas phase adsorbates above the surface. The integrated absorbance ratios are much higher at higher  $T$ , owing to disordered and rotating adsorbates, for example IAR = 0.70 for model E (compared to 0.33 at  $T = 30 \text{ K}$ ).

In summary, our calculations follow the observed experimental trends at low  $T$  for “C-down” species, *i.e.*, increasing IARs with increasing coverage (albeit not quantitatively), and they predict in addition, greatly enhanced IARs due to (i) CO inversion to “O-down” and/or (ii) high temperatures.

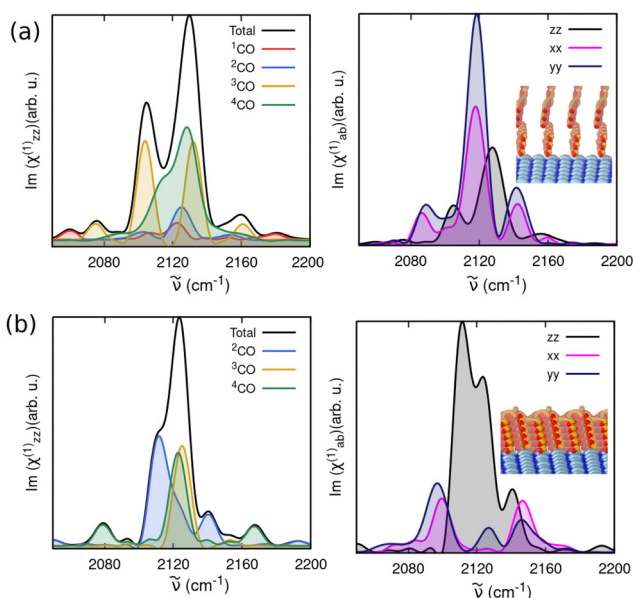


**Fig. 10** Computed IR spectral response of the CO/NaCl(100) system from trajectories starting from a 1 ML (a) P/U phase (model D), (b) one “O-bound” T/A phase configuration (model E), equilibrated at 300 K. The VVAFs leading to the spectra are averaged over five trajectories. Left panels show molecule-resolved and total spectra, right panels polarization-resolved total spectra with insets giving the same snapshots of AIMD trajectories as in Fig. 6.

We close this section by addressing the issue of Davydov splittings observed for CO/NaCl at low temperatures. All spectra so far were calculated with a resolution of  $11 \text{ cm}^{-1}$ , which is larger than the Davydov splitting of C–O stretch peaks of  $\Delta_D \sim 6 \text{ cm}^{-1}$ , observed for example for the 1 ML T/A phase at temperatures below 30 K.<sup>7</sup> In recent work, some of us have developed a machine-learned, neural network (NN) potential constructed from AIMD calculations similar to those here,<sup>12</sup> which allowed for  $t_{\text{sample}} = 16 \text{ ps}$  and a spectral resolution of *ca.*  $2 \text{ cm}^{-1}$  – enough to resolve the mentioned Davydov splittings. In ref. 12, at  $T = 5 \text{ K}$  trajectories were run on the trained NN potentials, showing indeed a Davydov splitting of the IR C–O stretch signal. More specifically, with the “Generation 6” NN potential, for the 1 ML T/A phases all “C-bound” (model C), one “O-bound” (model E), and all “O-bound” (model F), Davydov splittings of the peaks of 4.5, 3, and  $8 \text{ cm}^{-1}$  were found. These are in the correct order of magnitude for model C, and in addition predict a dependence of Davydov splittings if some or all CO molecules are inverted (models E and F).

### 3.5 Vibrational sum frequency (VSF) spectra

We also simulated VSF responses in the CO-stretch region for CO/NaCl, again, for different coverages, adsorbate orientations and temperatures, which so far have not been reported experimentally or theoretically for this system. Note that similar to the IR response, VSF spectra reported below were computed by the parametrized VVCF formulations that include angle-dependent dipole and polarizability derivatives, eqn (5) (without cross-correlations) or (7) (with cross-correlation). A comparison with the original formulation of Ohto *et al.*,<sup>25</sup> eqn (4) can be found in the ESI,<sup>†</sup> Section S3.3. As mentioned earlier, we also did not consider Fresnel factors and averaging, and rather show as a measure for an ssp-polarized VSF signal  $|\chi_{xxz}^{(2)}|^2$ , as well as  $\text{Im}\{\chi_{xxz}^{(2)}\}$  as the absorption response corresponding to the dissipative part as well as  $\text{Re}\{\chi_{xxz}^{(2)}\}$ , the dispersion response.

In Fig. 11, we show  $|\chi_{xxz}^{(2)}|^2$ ,  $\text{Im}\{\chi_{xxz}^{(2)}\}$ , and  $\text{Re}\{\chi_{xxz}^{(2)}\}$  for two 1 ML CO/NaCl(100) models at  $T = 30 \text{ K}$ , namely T/A all “C-bound” (model C), Fig. 11(a), and T/A one “O-bound” (model E), Fig. 11(b) respectively. Solid curves give total (black) and molecule-resolved (coloured) signals, and both the results without cross-correlations (eqn (5), dashed curves) and with cross-correlations (eqn (7) solid curves) are shown.

The 1 ML CO/NaCl(100) with all “C-bound” CO configuration without cross-correlations gives a total VSF signal for the CO stretch at  $2128 \text{ cm}^{-1}$  (Fig. 11(a), upper panel, dashed), similar to IR and VDOS responses. The corresponding  $\text{Im}\{\chi_{xxz}^{(2)}\}$  signal (Fig. 11(a), middle panel) shows a negative signal. For the one “O-bound” configuration, the VSF response in Fig. 11(b), upper panel, yields a CO stretch signal coming from “C-bound” molecules around  $2127 \text{ cm}^{-1}$ , and a red-shifted peak at  $2117 \text{ cm}^{-1}$ , giving an overall non-Lorentzian shape. In the imaginary response, the “C-bound” CO(s) yield a negative peak, while the “O-bound” CO yields a positive peak, resulting in a total signal with sign change (Fig. 11(b), middle). As argued in the ESI,<sup>†</sup> Section S3.3, this sign change for “O-down” is due to a sign change of the dipole



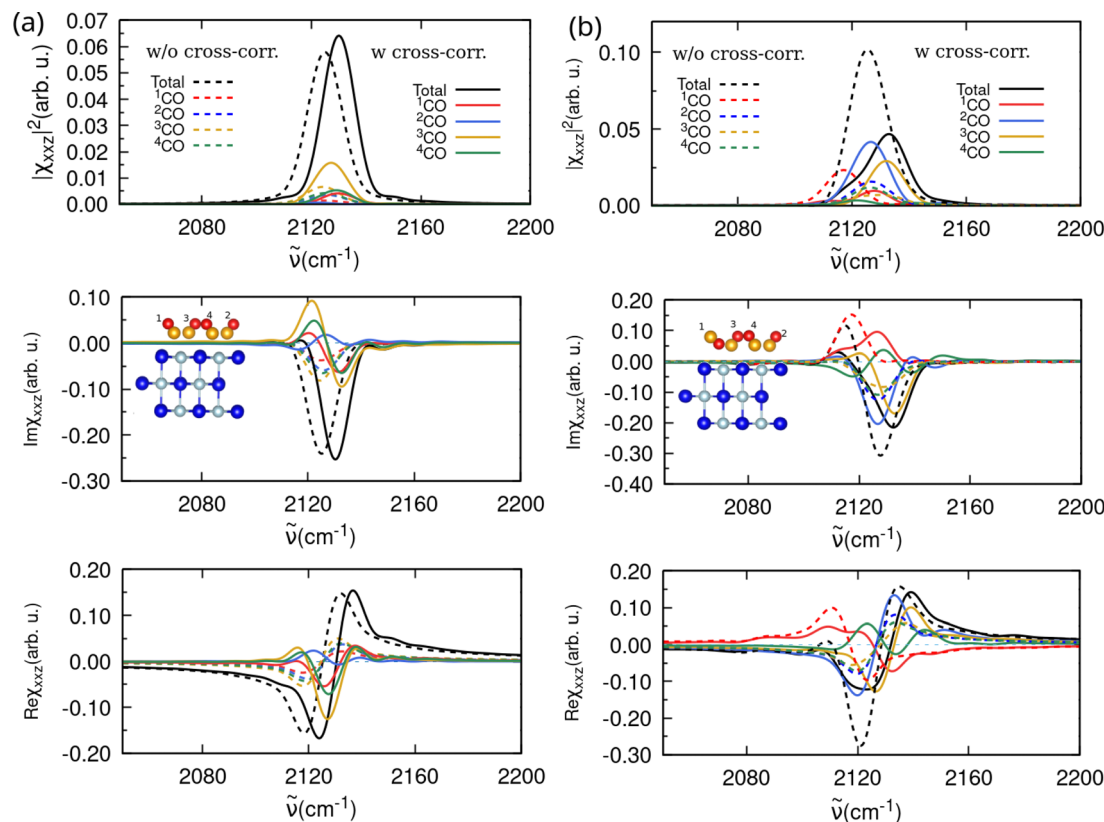


**Fig. 11** VSF spectra (intensity, imaginary and real responses) of (a) 1 ML T/A all “C-bound” CO/NaCl(100) (model C), and (b) T/A one “O-bound” CO/NaCl(100) (model E), at  $T = 30$  K. Spectra are calculated with angular-dependent, parametrized forms, either without cross-correlation terms (eqn (5), dashed) or with cross-correlations included (eqn (7), solid). Besides total (black), also molecule-resolved spectra (coloured) are shown.

derivative. When all adsorbed molecules are “O-bound”, we obtain a CO-stretch peak centered around  $2119\text{ cm}^{-1}$  and a corresponding positive peak in the imaginary response (not shown). Both the non-Lorentzian shape in (b), upper panel, and, even more so, the sign-change in the imaginary part in (b), middle panel, are characteristic signatures of a flipped CO molecule with “O-down”; they should be useful identifiers in VSF spectra. Differences between the one “O-down” and all “C-down” systems for real parts of  $\chi_{xxz}^{(2)}$  in the lower panels of Fig. 11 are less pronounced, and probably not well suited to identify flipped CO.

We note further from Fig. 11, solid curves, that the inclusion of cross-correlations in the correlation functions, eqn (7), has, for the present examples, the consequences that signals are blue-shifted (by typically  $\sim 10\text{ cm}^{-1}$ ), and that the asymmetry of the total VSF signal (upper panel of (b)) becomes more pronounced. We find also that introduction of cross-correlation terms, results in two peaks in the molecularly decomposed imaginary responses of all “C-down” ((a), middle panel, solid), making it harder to detect differences to the one “O-down” case ((b), middle panel, solid).

In summary, cross-correlations lead to blue-shifted VSF spectra (similar to IR), and to slightly different lineshapes at high (1 ML) coverages. In the ESI,† Section S3.3, we also report the VSF response at lower coverage (0.5 ML, model B) at  $T = 30$  K, using eqn (5) (angle-dependent dipole and polarizability

derivatives, Fig. S9, ESI†). When comparing this against spectra computed *via* eqn (4) (no angle-dependence), the differences between the two spectra are found to be negligible. Further, in Fig. S10 in the ESI,† Section S3.3, 1 ML P/U (model D) and 1 ML T/A one “O-bound” starting configurations (model E) were considered, at  $T = 300$  K. In this case, strongly reduced VSF intensities are found compared to  $T = 30$  K due to orientational disorder (and partial desorption) of CO at higher temperatures.

## 4 Conclusions and outlook

The primary emphasis of this study was in the simulation and analysis of vibrational spectra of CO at NaCl(100), for varying coverages, temperatures, and CO orientations. We aimed to provide insights into the structural and dynamic characteristics, using an AIMD-VVCF methodology. As a methodological aspect, we further attempted to explore effects of inclusion or non-inclusion, of orientational and cross-correlation in the correlation functions used for spectra evaluation. Some of our main findings are:

- We find strong dependence of vibrational signals on coverage and CO orientation (“C-down” *vs.* “O-down”), with higher coverages and “C-down” to “O-down” inversion causing



red-shifts, notably of C–O stretch modes, in agreement with experiments.

- At low temperature (30 K), CO molecules undergo only small-amplitude motions while at  $T = 300$  K, large-amplitude motions including roaming and desorption occur, with pronounced effects on spectra beyond simple line broadening. For example, a decrease in the coverage of CO molecules reduces dipole and multipole couplings between them; as a result coherence is lost, resulting in asymmetric tails and diffuse peaks in spectra.

- We have tested a modified formulation of the VVCF methodology with angle-dependent dipole and polarizability derivatives, and how it impacts the overall IR (integrated absorbance ratios) and the VSF response for situations where anisotropy of the dipole moment prevails. The inclusion of non-anisotropic terms in the VVCFs is particular important at higher temperatures. Then, also cross-correlations come into play, notably at high coverages.

- VSF spectra have been predicted for CO/NaCl which have the potential to give more direct insight into orientational dynamics compared to IR spectra, notably from imaginary parts of the VSF response.

- Insight into vibrational dynamics and mode couplings was also provided by distribution functions  $P(a)$ , and intra- as well as inter-molecular correlation distance matrices  $R(a,b)$ .

One possible extension of this work is to evaluate time-dependent transient spectra for non-equilibrium situations, for instance, pumping additional energy into the CO-stretch mode and follow how the energy redistributes into the neighbouring adsorbates and the NaCl surface. This has implications for various interesting phenomena the CO/NaCl(100) system is famous for, *e.g.* vibrational energy pooling and CO inversion and will appear soon in a follow-up publication.

## Data availability

The optimized geometries used as starting structures for the AIMD simulations are available in Zenodo under <https://doi.org/10.5281/zenodo.14356595>. Other AIMD data for vibrational spectra and analysis can be obtained upon reasonable request from the author.

## Conflicts of interest

There are no conflicts of interest to declare.

## Acknowledgements

We thank Giacomo Melani (Milano) for fruitful discussions on simulations of vibrational spectra, and Christopher Penschke (Potsdam) for help with computation of IR intensities of normal modes. We also thank David Picconi (Düsseldorf) for a useful suggestion about checking angular correlations. We thank the Deutsche Forschungsgemeinschaft (DFG) for support through project Sa 547/18-1 and the North-German

Supercomputing Alliance (HLRN) under the Nationales Hochleistungsrechnen (NHR) initiative for providing HPC resources. SS also thanks the International Max Planck Research School for Elementary Processes in Physical Chemistry for support.

## Notes and references

- 1 J. Heidberg, E. Kampshoff and M. Suhren, *J. Chem. Phys.*, 1991, **95**, 9408.
- 2 J. Vogt and B. Vogt, *J. Chem. Phys.*, 2014, **141**, 214708.
- 3 S. Picaud, P. N. M. Hoang, C. Girardet, A. W. Meredith and A. J. Stone, *Surf. Sci.*, 1993, **294**, 149–160.
- 4 A. D. Boese and P. Saalfrank, *J. Phys. Chem. C*, 2016, **120**, 12637–12653.
- 5 C. Noda and G. E. Ewing, *Surf. Sci.*, 1990, **240**, 181–192.
- 6 C. Noda, H. H. Richardson and G. E. Ewing, *J. Chem. Phys.*, 1990, **92**, 2099–2105.
- 7 D. Dai and G. Ewing, *Surf. Sci.*, 1994, **312**, 239–249.
- 8 J. A. Lau, A.-M. Schönemann, D. Schwarzer and A. M. Wodtke, *J. Chem. Phys.*, 2020, **153**, 154703.
- 9 J. A. Lau, A. Choudhury, C. Li, D. Schwarzer, V. B. Verma and A. M. Wodtke, *Science*, 2020, **367**, 175–178.
- 10 L. Chen, D. Schwarzer, V. B. Verma, M. J. Stevens, F. Marsili, R. P. Mirin, S. W. Nam and A. M. Wodtke, *Acc. Chem. Res.*, 2017, **50**, 1400–1409.
- 11 S. Corcelli and J. Tully, *J. Chem. Phys.*, 2002, **116**, 8079–8092.
- 12 S. Sinha, B. Mladineo, I. Lončarić and P. Saalfrank, *J. Phys. Chem. C*, 2024, **128**, 21117–21131.
- 13 A. Choudhury, S. Sinha, D. Harlander, J. DeVine, A. Kandratsenka, P. Saalfrank, D. Schwarzer and A. M. Wodtke, *Nat. Sci.*, 2023, **3**, e20230006.
- 14 L. Chen, J. A. Lau, D. Schwarzer, J. Meyer, V. B. Verma and A. M. Wodtke, *Science*, 2019, **363**, 158–161.
- 15 J. Chen, S. Hariharan, J. Meyer and H. Guo, *J. Phys. Chem. C*, 2020, **124**, 19146–19156.
- 16 S. Sinha and P. Saalfrank, *Phys. Chem. Chem. Phys.*, 2020, **23**, 7860–7874.
- 17 J. P. Perdew, K. Burke and M. Ernzerhof, *Phys. Rev. Lett.*, 1996, **77**, 3865–3868.
- 18 P. E. Blöchl, *Phys. Rev. B:Condens. Matter Mater. Phys.*, 1994, **50**, 17953–17979.
- 19 G. Kresse and J. Hafner, *Phys. Rev. B:Condens. Matter Mater. Phys.*, 1994, **49**, 14251–14269.
- 20 G. Kresse and J. Hafner, *Phys. Rev. B:Condens. Matter Mater. Phys.*, 1993, **47**, 558–561.
- 21 G. Kresse and J. Furthmüller, *Phys. Rev. B:Condens. Matter Mater. Phys.*, 1996, **54**, 11169–11186.
- 22 G. Kresse and J. Furthmüller, *Comput. Mater. Sci.*, 1996, **6**, 15–50.
- 23 S. Grimme, *J. Comput. Chem.*, 2006, **27**, 1787–1799.
- 24 S. Nosé, *J. Chem. Phys.*, 1984, **81**, 511–519.
- 25 T. Ohto, K. Usui, T. Hasegawa, M. Bonn and Y. Nagata, *J. Chem. Phys.*, 2015, **143**, 124702.
- 26 G. Melani, Y. Nagata, R. K. Campen and P. Saalfrank, *J. Chem. Phys.*, 2019, **150**, 244701.



- 27 P.-K. Lai and S.-T. Lin, *J. Comput. Chem.*, 2015, **36**, 507–517.
- 28 T. Yanai, D. P. Tew and N. C. Handy, *Chem. Phys. Lett.*, 2004, **393**, 51–57.
- 29 S. Grimme, J. Antony, S. Ehrlich and H. Krieg, *J. Chem. Phys.*, 2010, **132**, 154104.
- 30 M. J. Frisch, G. W. Trucks, H. B. Schlegel, G. E. Scuseria, M. A. Robb, J. R. Cheeseman, G. Scalmani, V. Barone, G. A. Petersson, H. Nakatsuji, X. Li, M. Caricato, A. V. Marenich, J. Bloino, B. G. Janesko, R. Gomperts, B. Mennucci, H. P. Hratchian, J. V. Ortiz, A. F. Izmaylov, J. L. Sonnenberg, D. Williams-Young, F. Ding, F. Lipparini, F. Egidi, J. Goings, B. Peng, A. Petrone, T. Henderson, D. Ranasinghe, V. G. Zakrzewski, J. Gao, N. Rega, G. Zheng, W. Liang, M. Hada, M. Ehara, K. Toyota, R. Fukuda, J. Hasegawa, M. Ishida, T. Nakajima, Y. Honda, O. Kitao, H. Nakai, T. Vreven, K. Throssell, J. A. Montgomery, Jr., J. E. Peralta, F. Ogliaro, M. J. Bearpark, J. J. Heyd, E. N. Brothers, K. N. Kudin, V. N. Staroverov, T. A. Keith, R. Kobayashi, J. Normand, K. Raghavachari, A. P. Rendell, J. C. Burant, S. S. Iyengar, J. Tomasi, M. Cossi, J. M. Millam, M. Klene, C. Adamo, R. Cammi, J. W. Ochterski, R. L. Martin, K. Morokuma, O. Farkas, J. B. Foresman and D. J. Fox, *Gaussian 16 Revision C.01*, Gaussian Inc., Wallingford CT, 2016.
- 31 G. J. Székely, M. L. Rizzo and N. K. Bakirov, *Ann. Stat.*, 2007, **35**, 2769–2794.
- 32 S. Heiden, D. Usvyat and P. Saalfrank, *J. Phys. Chem. C*, 2019, **123**, 6675–6684.
- 33 A. Nandi, P. Zhang, J. Chen, H. Guo and J. M. Bowman, *Nat. Chem.*, 2021, **13**, 249–254.

